Supplementary Information

Incipient nematicity from electron flat-bands in a kagomé metal

Nathan C. Drucker[1,2,†], Thanh Nguyen[1,3], Manasi Mandal[1,3], Yujie Quan [4], Artittaya Boonkird [1,3], Phum Siriviboon[1,5], Ryotaro Okabe[1,6], Fankgang Li[7], Kaleb Burrage[7], Fumiaki Funuma[7], Masaaki Matsuda[7], Douglas L. Abernathy[7], Travis Williams[7], Songxue Chi[7], Feng Ye[7] Christie Nelson[8], Bolin Liao[9,10], Pavel Volkov[9,10,†], and Mingda Li[1,3,†]

[1] *Quantum Measurement Group, MIT, Cambridge, MA 02138, USA*
[2] *John A. Paulson School of Engineering and Applied Sciences, Harvard University, Cambridge, MA 02138, USA*
[3] *Department of Nuclear Science and Engineering, MIT, Cambridge, MA 02139, USA*
[4] *Department of Mechanical Engineering, University of California, Santa Barbara, Santa Barbara, CA 93106, USA*
[5] *Department of Physics, MIT, Cambridge, MA 02139, USA*
[6] *Department of Chemistry, MIT, Cambridge, MA 02139, USA*
[7] *Neutron Scattering Division, Oak Ridge National Laboratory, Oak Ridge, TN 37831, USA*
[8] *National Synchrotron Light Source II, Brookhaven National Laboratory, Upton, NY 11973, USA*
[9] *Department of Physics, Harvard University, Cambridge, MA 02138, USA*
[10] *Department of Physics, University of Connecticut, Storrs, CT 06269, USA*

[†] Corresponding authors. ndrucker@g.harvard.edu, pavel.volkov@uconn.edu, mingda@mit.edu

Supplementary Note 1: Samples

We synthesized high-quality single crystals of CoSn through the Sn self-flux method. A mixture of Co chunks and Sn pellets were weighed in a molar ratio of 1:4 in a into a crucible. The mixture-filled crucible was flame-sealed in an evacuated quartz tube and was subsequently heated up to 400°C from room temperature at a rate of 100°C/h, then dwelled at 400°C for 2 hours. Next, the materials were heated to 950°C at 100°C/h and were then held at 950°C for 10 hours. The samples were then cooled to 650°C at a rate of 3°C/h, and were subsequently. This was followed by several days of annealing at this temperature after which centrifugation was performed to remove the excess flux.

The resulting products of CoSn single crystals are hexagonal prisms approximately half-centimeter long and have a metallic luster with lattice constants $a = b = 5.272$ Å and $c = 4.246$ Å as measured with single crystal neutron diffraction.

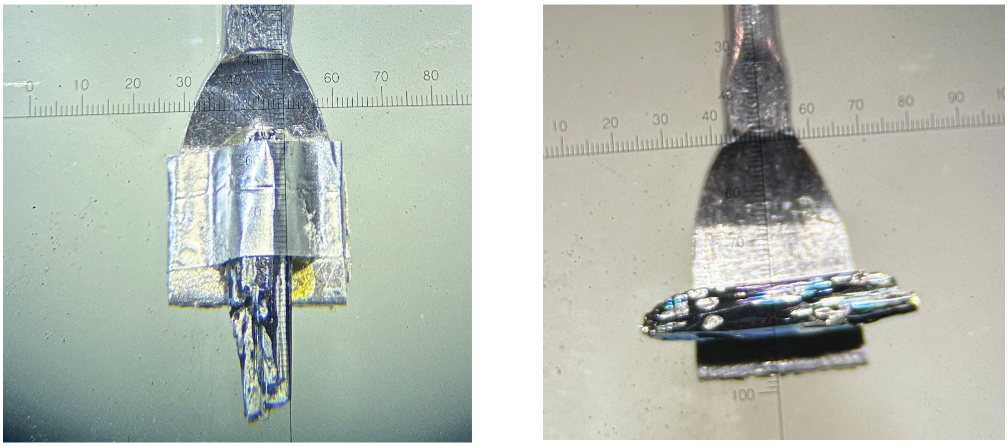

Supplementary Figure 1. Mounted CoSn single crystal for neturon diffraction. Image of CoSn single crystal mounted on an aluminum plate in preparation for elastic neutron diffraction. The lateral size of the crystal is ∼ 6 mm×2mm.

Supplementary Note 2: Electrical and thermal transport

Electrical and thermal transport were measured with the ETO and TTO modules of a QuantumDesign PPMS Dynacool system. Device contacts were made with silver epoxy H20E. For the thermal conductivity measurement, thermal gradient was applied along the c-axis of the material and thermometers were also placed along the c-axis. For the electrical transport measurements, the applied current along is the c-axis, voltage measured along the c-axis. The electrical and thermal transport are displayed in Supplementary Figure 2 on the left and right, respectively.

Supplementary Note 3: Heat capacity

Heat capacity measurements were taken with the Heat Capacity module of the Quantum Design PPMS Dynacool. The sample was mounted onto the stage with N-grease and the heat capacity was measured with the relaxation time method in addition to subtracting the addenda of the grease heat capacity. At each Temperature, the heat capacity was measured three times and averaged. To achieve different magnetic field directions, the sample was mounted in different orientations such that the field was applied along the [210] and [001] directions. The heat capacity measured for applied fields of 0 T and 9 T in the kagome plane are displayed in Supplementary Figure 3 on the left. On the right is shown the first derivative of heat capacity at zero field with respect to temperature, which is fit to a model of electronic, phononic, and anomalous contributions in the points and solid line, respectively.

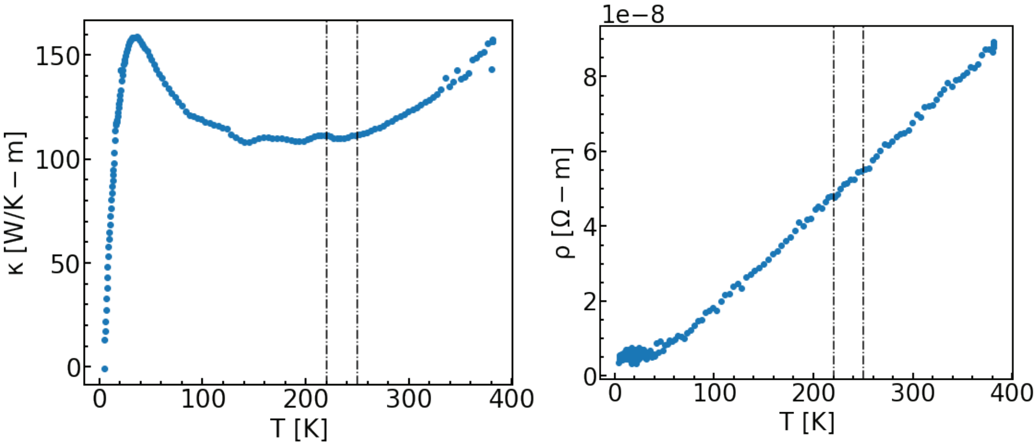

Supplementary Figure 2. CoSn Transport Left, thermal conductivity along the c-axis for thermal gradien along the c-axis measured from 2K to 300K. Right, Electrical resistivity for current and voltage direction along the c-axis, measured for temperatures from T=2K to T=300K. In each plot, dashed lines indicate boundary of anomalous behavior found in the thermoelectric measurement presented in the main text Figure 4.

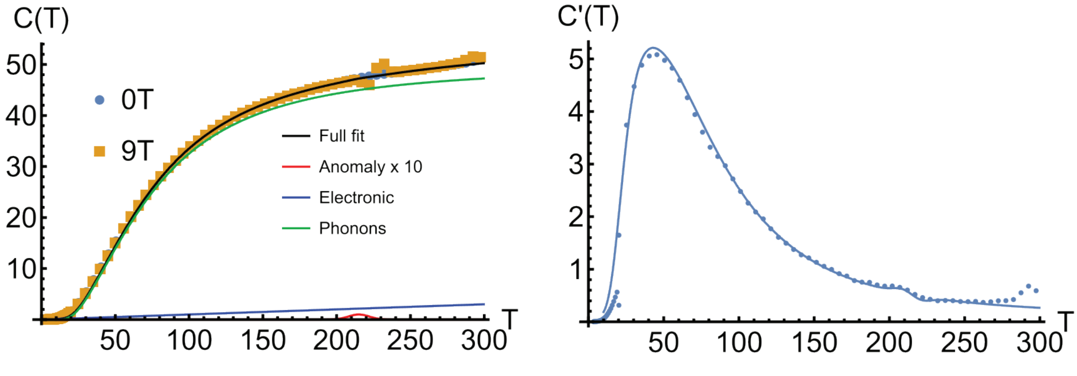

Supplementary Figure 3. Heat Capacity anomaly in zero field. Left, points represent experimentally measured heat capacity from T=2K to T=300K in fields applied within the kagome plane B=0T and B=9T. Solid lines indicate fits using a basic model phonon and electronic contributions to specific heat, with an additional small anomaly. Right, points are the numerical derivative of zero-field heat capacity data, and the solid line is the derivative of the model. There is a small kink in the derivative of the zero-field heat capacity near T=225K

Supplementary Note 4: REXS measurements

X-ray scattering measurements were carried out at the 4-ID beamline at NSLS-II. Single crystals were cleaved and mounted into the [H0L] scattering plane orientation with GE varnish and aligned to the [203] and [003] peaks. Temperature control was attained with a diplex closed cycle cryostat. The photon energy was selected to be at the Co K-edge, 7.709 keV. Energy scans with fixed Q from 7.6 keV to 7.8 keV at the [003] peak demonstrate the Co K-edge resonance. Subsequent meaurements were carried out at either 7.709 keV or 7.696 keV. Incoming polarization was fixed in the σ orientation, while outgoing polarization was detected in the σ' or π' channels via a Graphite (006) crystal analyzer. The scattering collected at the [003] peak in the $\sigma - \pi$' channel also shows a significant change with temperature through the anomaly at $T = 225$K.

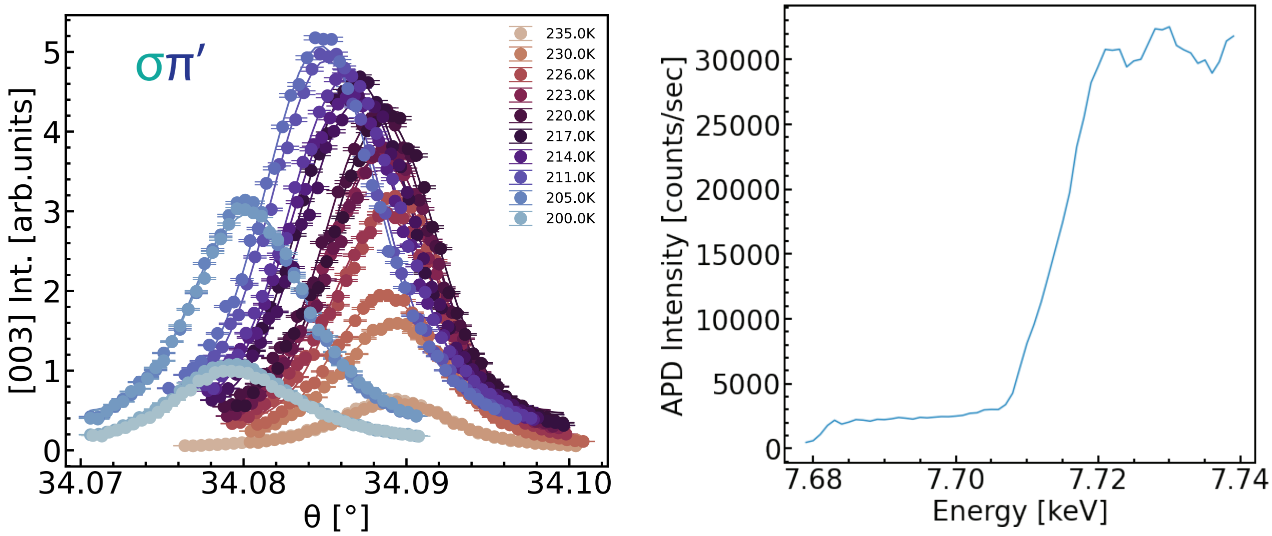

Supplementary Figure 4. REXS at the Co K-edge Left, rocking curves taken at temperatures near the anomaly for X-rays in the polarization-flip channel $\sigma\pi'$. Right, fluorescence scan near the Co K-edge measured at room temperature.

Supplementary Note 5: Anisotropic X-ray Structure Factor

When incident X-rays are resonant to an atomic transition, it becomes necessary to include higher order terms in the interaction between the photons and electrons in the sample. As a result, the so-called anomalous X-ray scattering factor (AXS) introduces additional terms on top of the standard Thompson scattering f_0 which arises from dipole-dipole scattering $f(E) = f_0 + f'(E) + if''(E)$ [1, 2]. These terms have quadrupole-quadrupole and dipole-quadrupole contributions. In addition to the AXS enhancement, scattering from anisotropic charge distributions can further modify the scattering cross-section, leaading to phenomena including but not limited to the observation of forbidden Bragg peaks near resonance (Templeton scattering). The consequence of the anisotropic charge distribution is that the scattering factor $F(E,Q)$ becomes a tensor, rather than a scalar. This tensor must respect the underlying symmetry of the unit cell, and is thus sensitive to symmetry breaking. Such symmetry

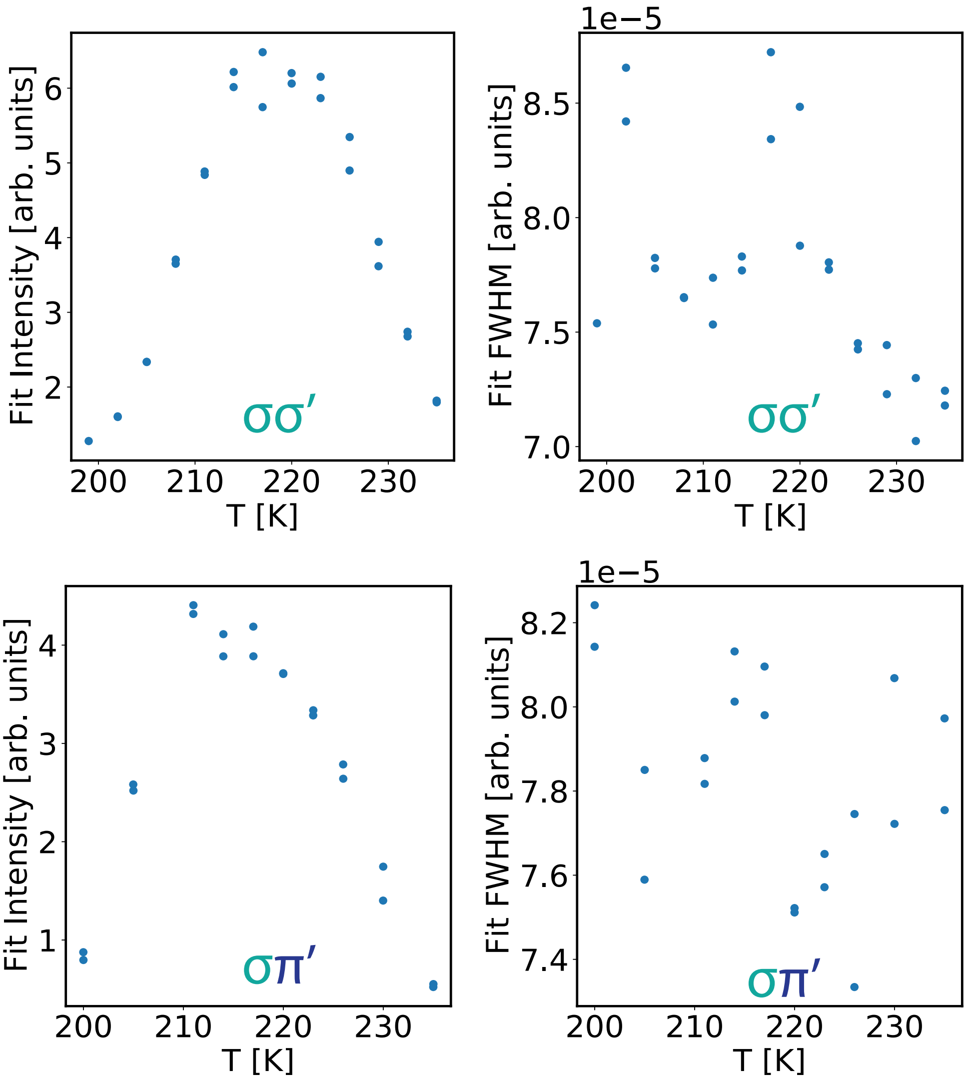

Supplementary Figure 5. REXS intensity and width through the anomaly [003] Peak maximum intensity (left) and full-width-half-max (right) based on Gaussian fits of the rocking curves taken in both polarization channels (top, bottom respectively).

breaking can be provided by magnetism, orbital order, or nematicity. In addition to the anomalous Scattering factor being energy dependent, it also depends on the azimuthal angle ψ between the incident X-rays and the motif that they scatter from. In sum:

$$F(E, Q, \psi) = \sum_n \varepsilon^i U(\psi) V_n F_n(E, Q) V_n^T U^T(\psi) \varepsilon^f$$

Where E is the incident photon energy, Q is the scattering momentum, n are the atoms in the unit cell, ψ is the relative angle between the lab frame and the crystallographic basis, and $\varepsilon^{i,f}$ are the incoming and outgoing X-ray polarizations. For the $\sigma\sigma'$ channel $\varepsilon^i = \varepsilon^f = (1, 0, 0)$, whereas for the $\sigma\pi'$ channel $\varepsilon^i = (1, 0, 0)$ and $\varepsilon^f = (0, 0, 1)$ The U and V matrices are rotations between the lab-frame and crystal coordinates, and orbital motif and crystal coordinates, respectively.

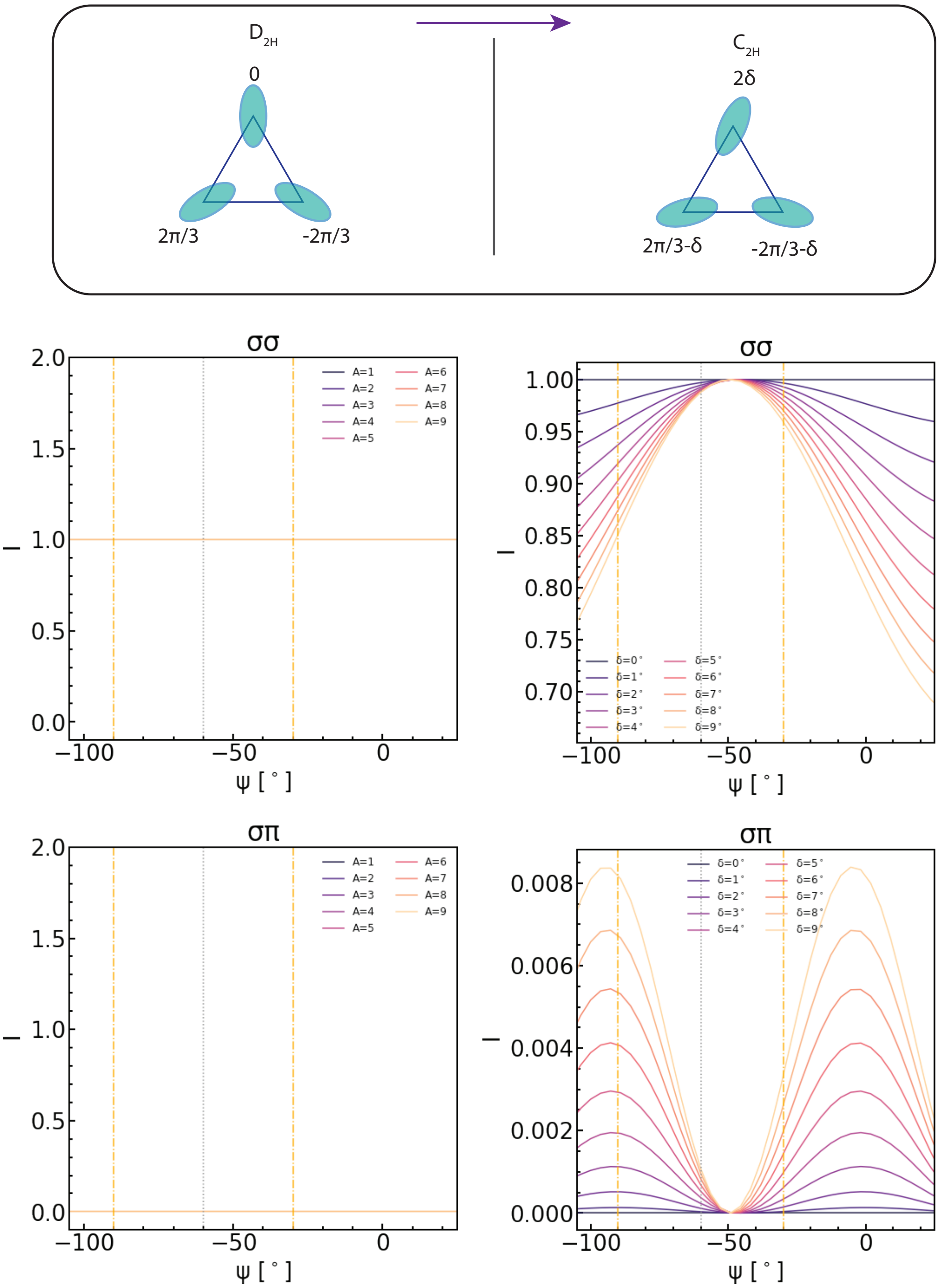

Supplementary Figure 6. Modeling anomalous X-ray scattering Azimuthal dependence of the REXS intensity in different polarization channels for an undistorted (left) and nematic (right) charge distribution. Note that even when the charge distrubition is anisotropic but there is no nematicity, there is no Azimuthal dependence on the scattering intensity.

Because of the anomalous X-ray efffect, F_n is a diagonal tensor in the basis of the (orbital) motif:

$$F_n(E,Q) = \begin{pmatrix} F_{xx} & 0 & 0 \\ 0 & F_{yy} & 0 \\ 0 & 0 & F_{zz} \end{pmatrix}$$

In the isotropic case within the xy plane, $F_{xx} = F_{yy}$. In the anisotropic case (within the a-b plane), we can parameterize the in-plane anisotropy as a factor $a = F_{xx}/F_{yy}$.

$$F_n(E, Q) = \begin{pmatrix} a & 0 & 0 \\ 0 & 1 & 0 \\ 0 & 0 & c \end{pmatrix}$$

To construct the scattering intensity as a function of asymmetry a at the [003] scattering peak, we simply use the formula for total structure factor from the Co atoms. We note that even though the scattering vector Q does not have an in-plane component, the total Intensity still depends on the in-plane structure factors due to the phase factor.

$$I(Q) = \left| \sum_n F'_n(Q) e^{iQ\cdot R_n} \right|^2$$

Where $Q = [003]$ and R_n are the three sites of the Co atoms in the unit cell and $F'_n(Q)$ is the structure factor after the proper rotations defined above. An example of this motif that is anisotropic at the Co site is shown in SI Figure 6. While the anisotropy changes the total magnitude of the scattering factor, note that it alone does not break the rotational symmetry of the unit cell, and thus does not induce an azimuthal dependence in either the $\sigma\sigma'$ or the $\sigma\pi'$ polarization channels. We can model the rotational symmetry breaking by introducing an angular perturbation to the anisotropic Co sites, which introduces an azimuthal dependence of both polarization channels.

This azimuthal dependence is explicitly shown for the two cases in SI figure 6, based on numerical calculations of the total Intensity I(Q) defined above. This dependence can also be worked out analytically for arbitrary perturbations δ_i and anistropy factor a for each Co site i in the unit cell. It can be shown that

$$\delta I_{\sigma\sigma'} \propto [2\delta_1 - \delta_2 - \delta_3](1-a)\sin 2\psi + [\delta_2 - \delta_1]\sqrt{3}(a+1)\cos 2\psi$$

$$\delta I_{\sigma\pi'} \propto (1-a)^2[(2\delta_1 - \delta_2 - \delta_3)\cos 2\psi + [\delta_2 - \delta_3]\sqrt{3}\sin 2\psi]^2$$

The $\sigma\sigma'$ polarizaiton channel is two-fold symmetric whereas the $\sigma\pi'$ is four-fold symmetric. For small δ_i the $\sin 2\psi$ term in $\sigma\sigma'$ dominates and the azimuthal dependence is peaked near $\psi = \pi/4$. These analytical results are confirmed through the numerical calculations shown in SI Figure 6, and also are corroborated by the data in the main text Figure 3, where the azimuthal intensity in the $\sigma\sigma'$ channel is two-fold and peaked near $\psi = \pi/4$.

Experimentally, the azimuthal scans were performed by rotating the sample azimuth, and then optimizing the peak position at each azimuthal angle to correct for possible translations of the beam relative to the the sample and additional tilting effects.

Supplementary Note 5: Single Crystal Neutron Diffraction

Single crystal neutron diffraction experiments were done at the BL-9 CORELLI instrument at the Spallation Neutron Source (SNS) of Oak Ridge National Lab. A single crystal of 80 mg was loaded into the instrument with two different orientations, one with the (HK0) scattering orientation and the other along the (H0L) scattering orientation. The samples were cooled in zero field to temperatures of 150K, 220K, and 300K. At each of these temperatures, a magnetic field of 4.75 T was applied perpendicular to the c-axis and parallel to the c-axis for the H0L and HK0 orientations, respectively.

The diffraction patterns for the (HK0) and (H0L) planes are shown in Supplementary Figures 7 and 8, respectively. To within the resolution of the instrument of $\Delta Q/Q \sim 1e-3$, there is not an apparent change in the structure as temperature is cooled or field is changed. In neither the (H0L) plane nor the (HK0) planes are there peaks other than the structural Bragg peaks. This lack of new peaks around the Bragg positions agrees with the hypothesis that the anomalies are not due to emergent magnetic or charge density wave orderings.

Supplementary Note 6: Ab-initio Molecular Dynamics Calculations

To capture the renormalized phonon dispersions at finite temperature, the temperature-dependent interatomic force constants (IFCs) were extracted by combining ab initio molecular dynamics (AIMD) simulations and the temperature-dependent effective potential (TDEP) technique [3, 4]. The AIMD simulations were performed within the density functional theory (DFT) framework implemented in the Vienna Abinitio Simulation Package (VASP) [5–7]. The simulations used the projector-augmented wave formalism [8] with exchange-correlation energy functional parameterized by Perdew, Burke, and Ernzerhof within the generalized gradient approximation [9]. Before AIMD simulations, the crystal structure was fully relaxed with energy and Hellmann–Feynman force convergence thresholds of 10^{-6} eV and 10^{-4} eV/Å, respectively, and the difference between the optimized lattice constants and the experimental values is within 1%. The AIMD simulations were performed on a 3×3×3 supercell, 162

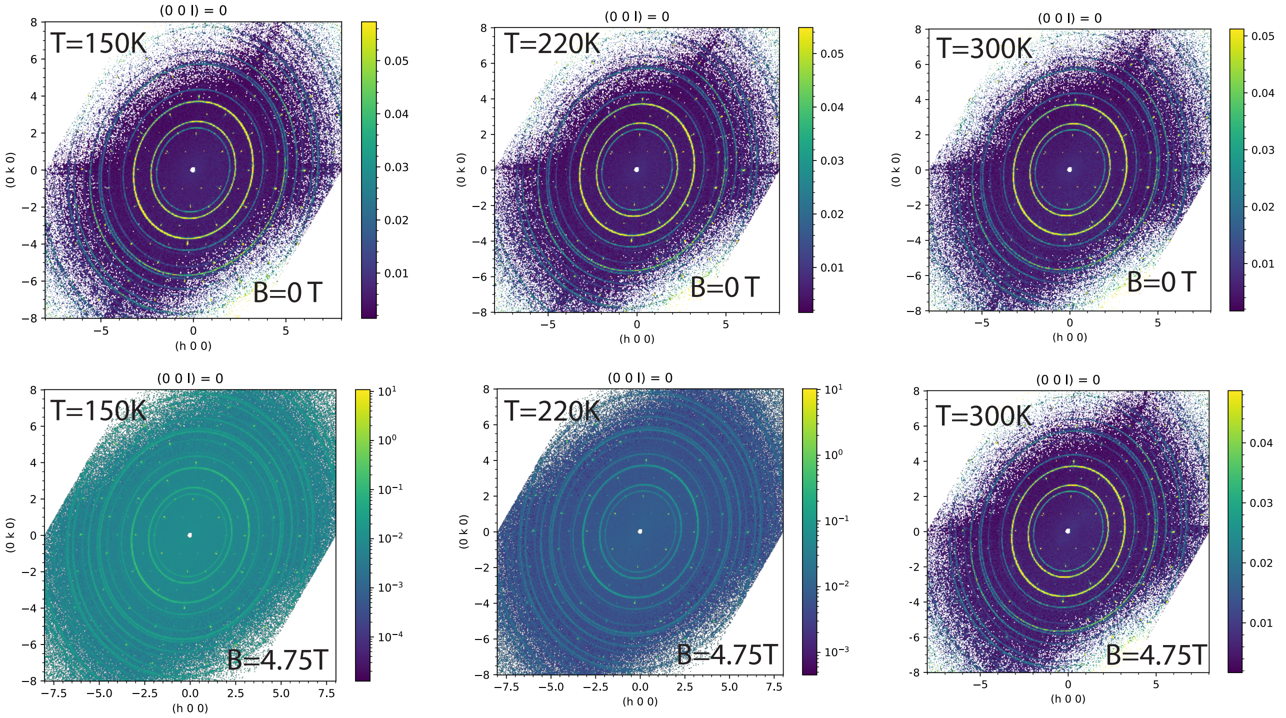

Supplementary Figure 7. Neutron diffraction in the (HK0) plane. Time of flight neutron diffraction patterns at temperatures of 150K, 220K, 300K left, right, middle) and magnetic field of 4.75 T (top, bottom, respectively). Within the (HK0) scattering plane, there are only structural Bragg peaks resolved, confirming the lack of space group change, magnetic order, or cdw order.

atoms in total. The electronic self-consistent loop convergence was set to 10^{-5} eV. A single Γ-point k-mesh with a plane-wave cut-off energy of 350 eV was used to fit the effective energy surface using the TDEP method. The simulations were performed at 200, 210, 220, 230, 240, 250, and 300 K, with the NVT ensemble using a Nose–Hoover thermostat. All the simulations were run for 10 ps with a timestep of 2 fs, and the initial 1 ps's information was discarded due to the nonequilibrium.

Supplementary Note 7: Inelastic Neutron Scattering

Inelastic neutron scattering measurements were performed at Oak Ridge National Laboratory (ORNL). Specifically the triple-axis measurements were carried out at the HB3 beamline at the High Flux Isotope Reactor (HFIR) and the time-of-flight measurements were carried out at the ARCS beamline at the Spallation Neutron Source (SNS). HFIR experiments were carried out by selecting a final scattered neutron energy of E_f = 14.7 meV and varying the incident neutron energy in constant Q mode. Horizontal collimation settings of 48'-40'-Sample-40'-120' were used. ARCS measurements were done with incident neutron energy of $E_i = 35$ meV.

Supplementary Note 8: Magnetostriction

Magnetostiction experiments were performed with a commercially available mini-dilatometer [10] which is compatible with the sample environment provided by the Quantum Design PPMS. This device can

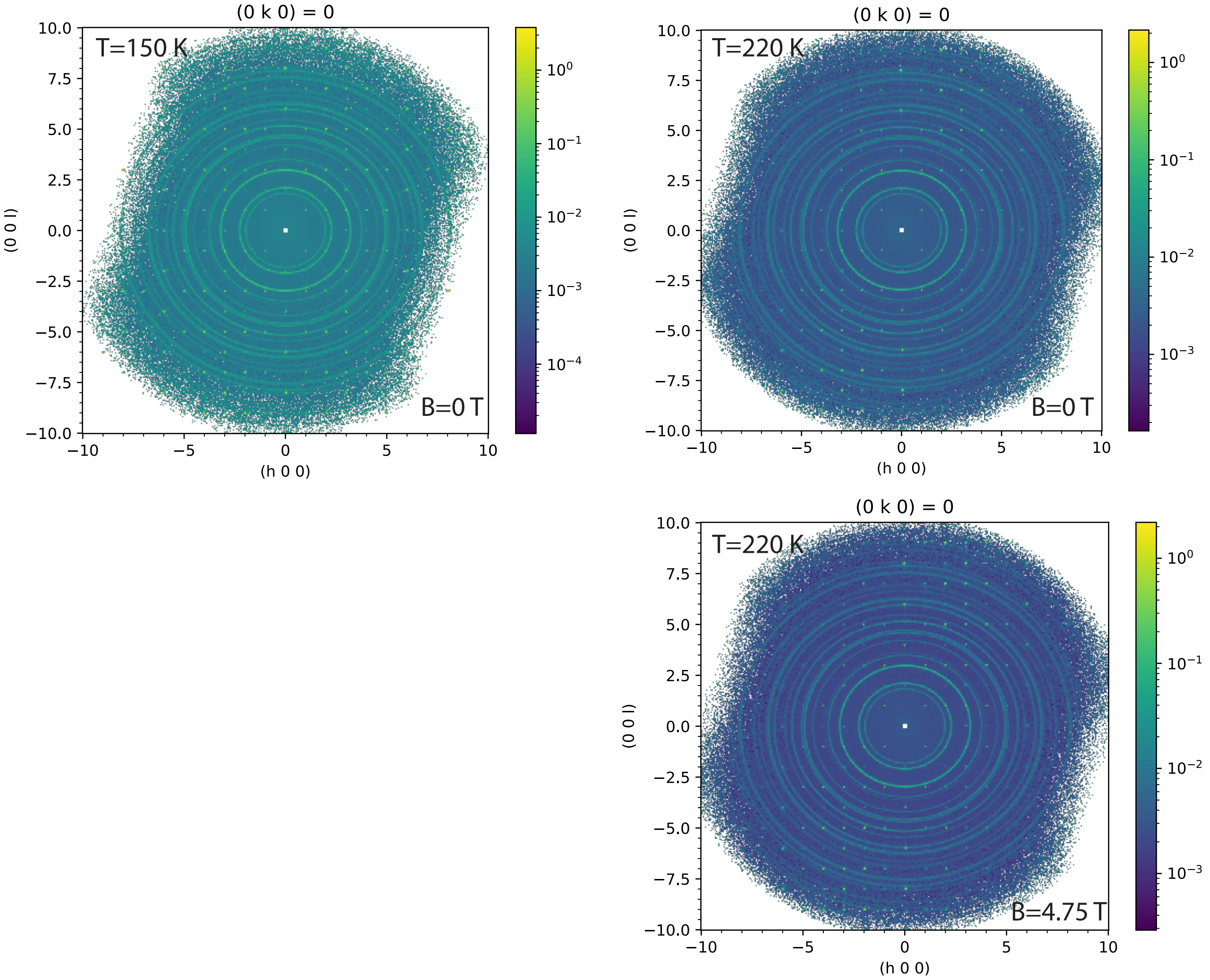

Supplementary Figure 8. Neutron diffraction in the (H0L) plane. Time of flight neutron diffraction patterns at temperatures of 150K and 220K (left, right respectively). Within the (H0L) scattering plane, there are only structural Bragg peaks resolved, confirming the lack of space group change, magnetic order, or cdw order.

be rotated relative to the applied magnetic field to find the magnetostriction for field applied along specific crystallographic axes. The sample was mounted such that the change in length was measured along the [210] direction for fields applied along the [110] and [010] directions. The resulting dilation at measured at different temperatures can be fit based on the phenomenological model derived above such that

$$\Delta L/L \propto a + bH^2 + cH^4$$

where a, b, and c are constants and H is the value of applied magnetic field. Fits to this model at higher magnetic field values are shown in red in SI Figure 11. For each direction, the extracted coefficient to the H^2 term are plotted as a function of temperature in SI Figure 11. At T= 235 K there is a kink in the coefficient's behavior, and below this temperature b is negative for the field along the [010]

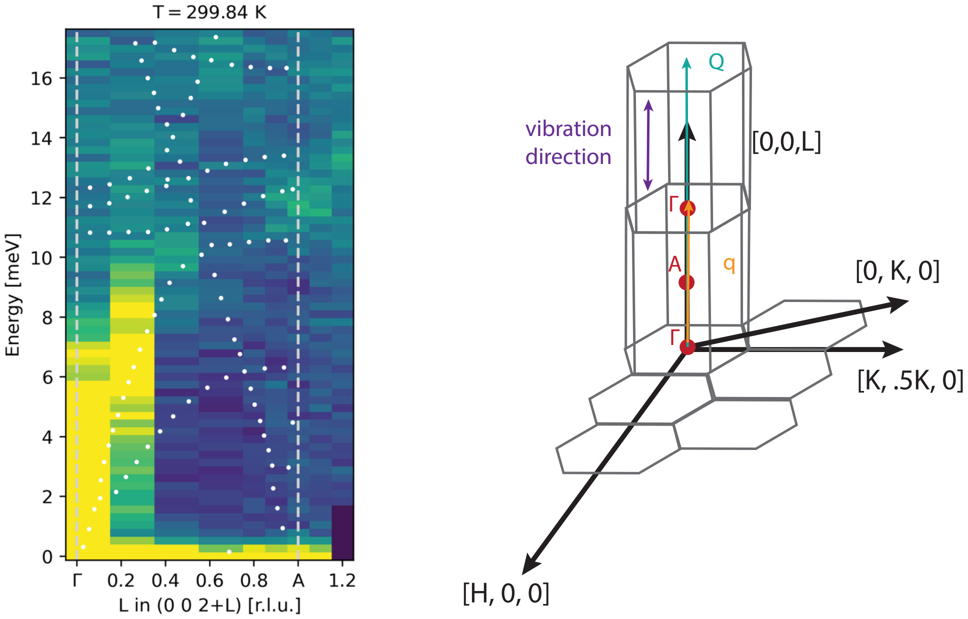

Supplementary Figure 9. Inelastic Neutron scattering from transverse phonons. Left, phonon bandstructure along the $\Gamma - A - \Gamma$ direction measured with triple axis spectroscopy along the 00L direction. White dotted lines are overlayed from the AIMD calculations of the phonon bandstructure at this temperature. Right, schematic of scattering geometry with neutron momentum Q, phonon wavevector q, and the resulting vibration direction indicated with teal, orange, and purple arrows respectively In contrast to the INS measurements shown in main text, the vibration direction of these phonons is transverse relative to the kagome plane.

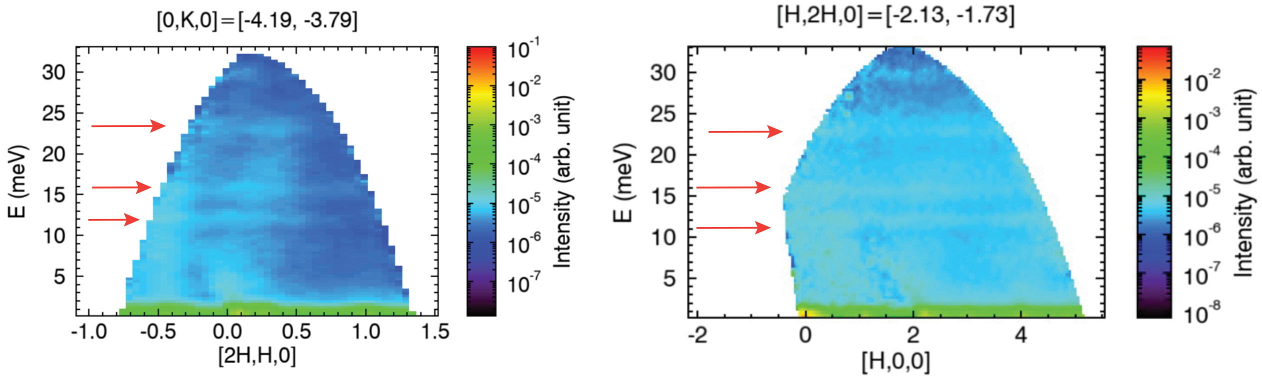

Supplementary Figure 10. Phonon bandstructure from time-of-flight measurements. Inelastic neutron scattering measurements of the phonon band structure using the time-of-of flight method at the Spallation Neutron Source reveal flat phonon bands, indicated by the orange arrows. Left and right panels depict two different directions in reciprocal space. The phonons are flat across multiple Brillouin zones.

direction but positive for field along the [110] direction. We also construct a proxy value η for the nematicity based on these coefficients

$$\eta = \frac{b_{[010]} - b_{[110]}}{b_{[010]} + b_{[110]}}$$

Which is plotted in red. Note that near $T^* = 225K$, this value approaches diverges but approaches zero, at temperatures away from this value. There is another divergence near T = 240 K that arises when the denominator of η diverges.

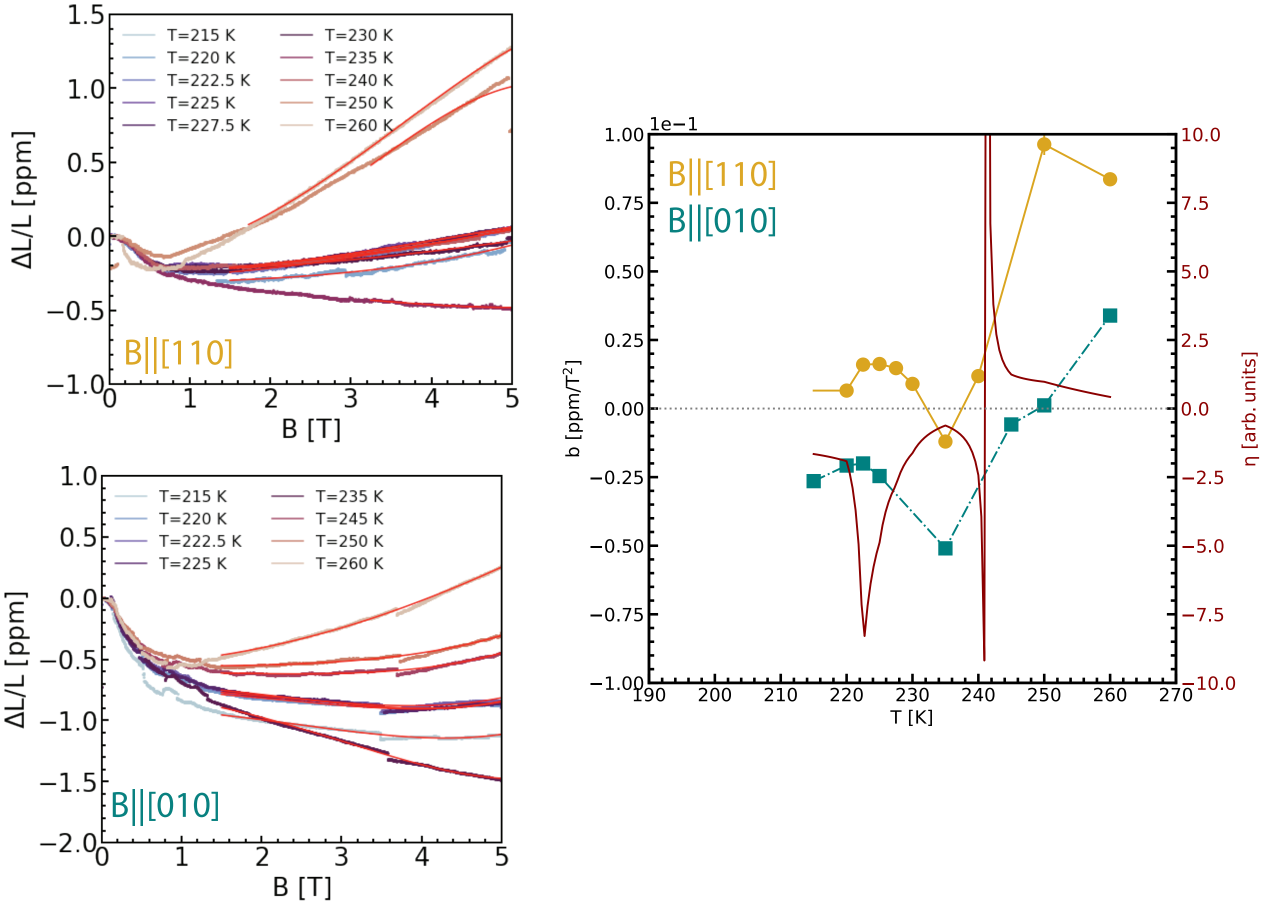

Supplementary Figure 11. Magnetostriction scaling. Right, magnetostriction along the [210] direction for fields applied along the [110] and [010] directions top and bottom, respectively for different temperatures through the anomaly. Solid red lines indicate a fit to $\Delta L/L = a + b * B^2 + c * B^4$ as predicted from first principles. Right, coefficient of the square term b for each field direction in yellow and teal respectively along with a nematicity parameter $\eta = (b_{[110]} - b_{[010]})/(b_{[110]} + b_{[010]})$ in dark red.

Supplementary Note 9: Neutron Larmor Diffraction

High resolution neutron Larmor diffraction was used to measure the lattice spacings along different crystallographic directions[11, 12] at the HB-1 beamline at the High Flux Isotope Reactor (HFIR) at Oak Ridge National Laboratory [13]. This technique depends on the change in Larmor phase ϕ of polarized neutrons subjected to a magnetic field B before and after scattering from a single-crystal sample. The measured Larmor phase is

$$\phi = \frac{\gamma_N m d B L}{2\pi h}$$

Where γ_N is the gyromagnetic ratio of the neutron, m is the neutron mass, d is the lattice spacing, B is the field strength and L is path length of the field. In this way, small changes in the lattice spacing d are detectable by a change in Larmor phase ϕ.

Coaligned samples were oriented in different scattering geometries in order to measure along the [201], [021], and [002] directions.

One advantage of this technique is that a change in the total magnitude of ϕ can detect structural phase transitions [11, 13] up to a resolution of $\Delta d/d = 1e-5$. In our measurements, there was not a significant change in the overall magnitdue of ϕ at temperatures near T$^* = 225$K as shown in SI figure 13.

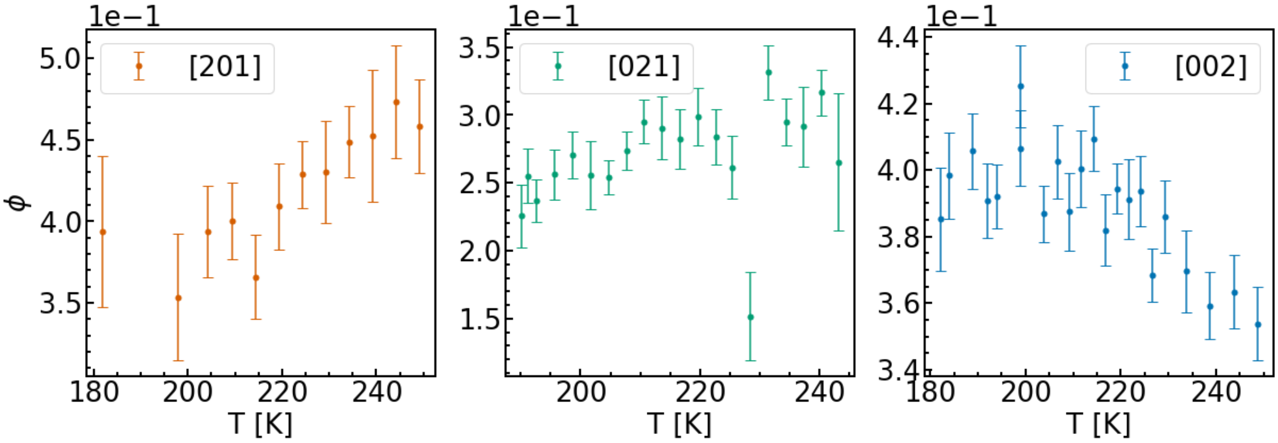

Supplementary Figure 12. Larmor diffraction amplitude. Total neutron Larmor phase amplidude at different temperatures through the nematic region for different crystallographic orientations. The lack of sharp change in the Larmor phase amplitude suggests that a structural phase transition is not detected despite the change in lattice distortion.

Supplementary Note 10: Thermodynamics and susceptibility of a Kagome lattice model

Here we show that susceptibility of flat-band electrons in a Kagome lattice shows a pronounced peak at an intermediate temperature. We follow the notation of [14]:

$$H(\mathbf{k}) = E_0 + \begin{pmatrix} 0 & t_1 + t_1 e^{-2ik_x a} & t_2 + t_2 e^{-i(kx+\sqrt{3}ky)a} \\ t_1 + t_1 e^{-2ik_x a} & 0 & t_3 + t_3 e^{-i(-kx+\sqrt{3}ky)a} \\ t_2 + t_2 e^{i(kx+\sqrt{3}ky)a} & t_3 + t_3 e^{i(-kx+\sqrt{3}ky)a} & 0 \end{pmatrix}, \tag{1}$$

where in the absence of distortions $t_1 = t_2 = t_3 = t$.

Strain deforms the Kagome lattice, such that $t_{1,2,3}$ become non-equivalent [14]. For example, ε_{xx} strain results in

$$t_1 = t,\ t_2 = t + \alpha,\ t_3 = t + \alpha, \tag{2}$$

where $\alpha \propto \varepsilon_{xx}$.

The action of B_{1u} deformation is to bring three atoms closer to the center of hexagons, ultimately forming trimers (see Fig. 5 (c) of main text). This can be modeled by an increase/decrease in nextnearest-neighbor tunneling strengths as follows:

$$\delta H_{B_{1u}}(\mathbf{k}) = \delta \begin{pmatrix} 0 & e^{i(-k_x+\sqrt{3}k_y)} - e^{i(-k_x-\sqrt{3}k_y)} & e^{-2ik_x} - e^{i(k_x-\sqrt{3}k_y)} \\ e^{-i(-k_x+\sqrt{3}k_y)} - e^{-i(-k_x-\sqrt{3}k_y)} & 0 & e^{i(-k_x-\sqrt{3}k_y)} - e^{2ik_x} \\ e^{2ik_x} - e^{-i(k_x-\sqrt{3}k_y)} & e^{-i(-k_x-\sqrt{3}k_y)} - e^{-2ik_x} & 0 \end{pmatrix}, \tag{3}$$

In Fig. 5 of the main text we show the band structure cut and density of states for (a) $t_1 = t_2 = t_3 = -1$, (b) $t = -1, \alpha = 0.1$ (c) $t = -1, \delta = -0.2$. The results were calculated numerically, using 512x512 k-points in the Brillouin zone and Lorentzian energy smearing of each eigenstate with width $0.01t$. For both distortions, the most dramatic effect is the smearing of the density of states peak due to the flat band.

In Fig. 13 we show the dependence of the top band's width and its averaged energy as a function of α or δ. For strain (α), there is a dramatic increase of the flat band width, that is linear in α, while B_{1u} distortion leads to a quadratic increase. In both cases the average energy of the flat band shifts, but for strain the dependence is less well described by quadratic; the fit shown in Fig. 13 (a) is of the form $ax^2 + bx^4$, while it is purely quadratic in (b).

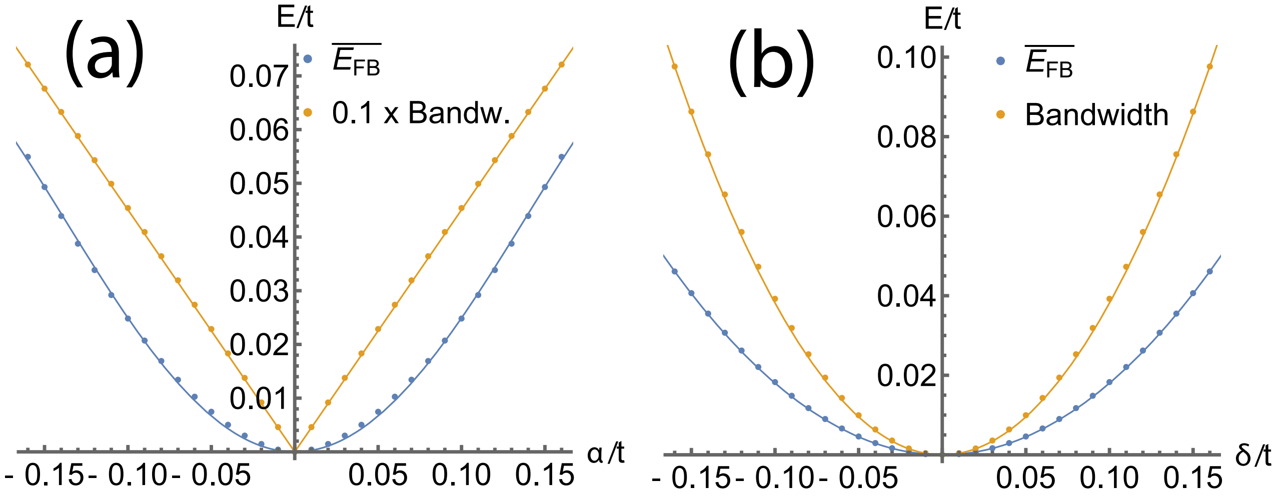

Supplementary Figure 13. Change of the flat band parameters for distorted Kagome model (a) Effect of strain (b) B_{1u} distortion. Lines are polynomial fits to the numerical points.

Let us now consider the temperature dependence of the system's susceptibility to such distortions. We compute numerically the free energy with and without the distortion including full band structure of the model, Eq. (1),(3).

$$\begin{aligned} \chi_\alpha = -\frac{\partial^2 F}{\partial \alpha^2}; \quad \chi_\delta = -\frac{\partial^2 F}{\partial \delta^2} \\ F(T,\alpha,\delta) = -2T\sum_{\mathbf{k}} \log\left[\prod_{i=1}^{3}(1+e^{-E_i(\mathbf{k},\alpha,\delta)/T})\right], \end{aligned} \tag{4}$$

where $E_i(\mathbf{k})$ are the egenvalues for the distorted Kagome models described above.

Fig. 14 shows the susceptibility calculated numerically on a 128x128 momentum grid and with the derivative approximated by $\frac{\partial^2 F}{\partial x^2} \approx [F(x)+F(-x)-2F(0)]/(2x^2)$ taken for $x \equiv \delta = 0.01$ and $x \equiv \alpha = 0.01$. To analyze the results we further separate the contribution arising from the flat band acquiring a finite bandwidth due to distortion, see Fig. 13. It is equal to:

$$\begin{aligned} \chi_\alpha^{FB} = -\frac{\partial^2 F^{FB}}{\partial \alpha^2}; \quad \chi_\delta^{FB} = -\frac{\partial^2 F^{FB}}{\partial \delta^2}, \\ F(T,\alpha,\delta) = -2T\sum_{\mathbf{k}} \log\left[(1+e^{-\frac{E_{FB}(\mathbf{k},\alpha,\delta)-\overline{E}_{FB}(\alpha,\delta)}{T}})\right]. \end{aligned} \tag{5}$$

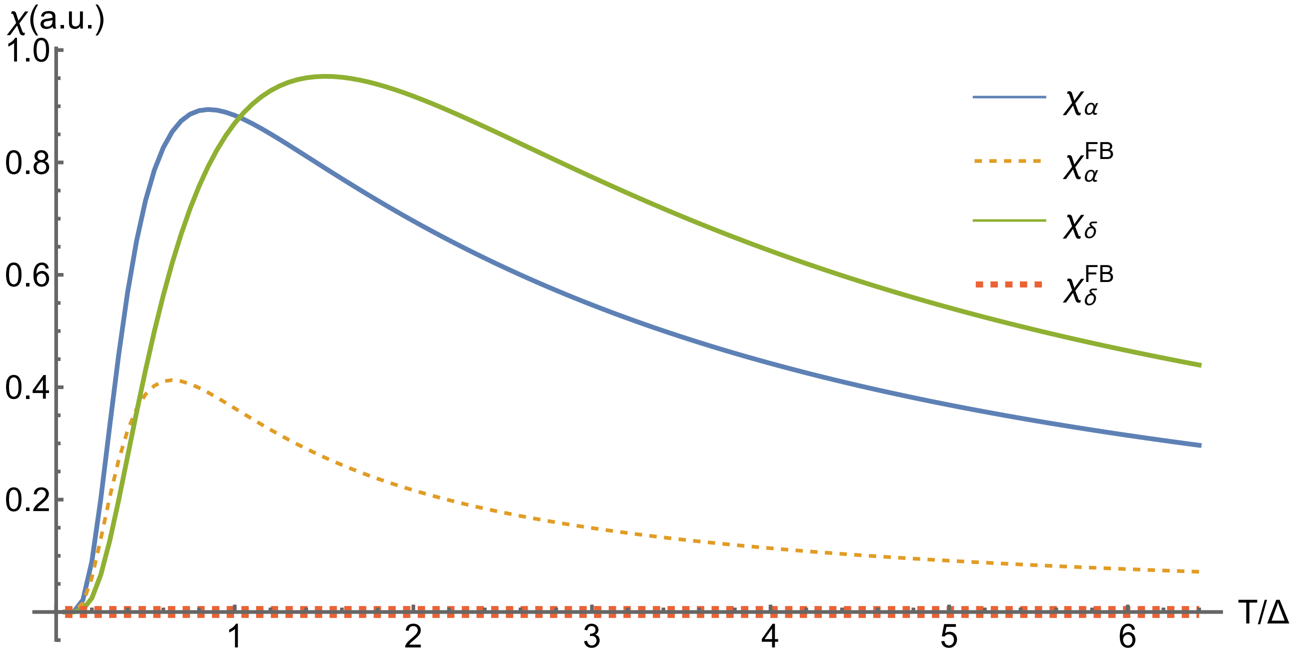

Supplementary Figure 14. Kagome model susceptibilities. Solid lines are the susceptibilities, Eq. (4) with respect to strain (blue) and B_{1u} distortion (green). Dashed lines represent the contribution of the flat band broadening to susceptibility, Eq. (5).

One observes that both susceptibilites have a peak at a finite T smaller then the gap value. For strain, a significant part of susceptibility can be attributed to the increasing dispersion of the flat band. The rest is due to shifts in average position of the bands and in principle should be less universal. Note that the flat band broadening does not contribute to the B_{1u} susceptibility.

To capture the response due to broadening of the flat band that is expected to be more universal one can consider the following simplified model. For non-zero α, we approximate the density of states as a "box" with a finite width equal to $c\alpha$. Then, the free energy per unit cell takes then the form:

$$\begin{aligned} F_{mod} = -T \int_{-\Delta-c\alpha/2}^{-\Delta+c\alpha/2} \frac{d\varepsilon}{c\alpha} \log[1+e^{-\frac{\varepsilon}{T}}] \approx -T\log[1+e^{\frac{\Delta}{T}}] \\ -\frac{e^{\frac{\Delta}{T}}}{24T(1+e^{\frac{\Delta}{T}})^2} c^2\alpha^2 + O(\alpha^4) \end{aligned} \tag{6}$$

From the above one extracts the expression for susceptibility given in the main text.

Supplementary Note 11: Specific heat for phenomenological model

The specific heat obtained from the free energy given in the main text is:

$$\delta C = -T\frac{\partial^2 F}{\partial T^2} \approx \frac{2T^*(G_\Phi(T^*)\vec{\sigma}^2 - 2G\vec{\kappa}\cdot\vec{\sigma})}{|G''_\Phi(T^*)|G_\varepsilon} \frac{3(T-T^*)^2 - T'^2}{(T-T^*)^2 + T'^2}, \tag{7}$$

where we denote $T' = \frac{2}{|G''_\Phi(T^*)|}[G^2/G_\varepsilon - G_\Phi(T^*)]$.

We can parametrize the result as $\delta C = C_0(1+a\kappa)\frac{3(T-T^*)^2-T'^2}{(T-T^*)^2+T'^2}$

The function plotted in Fig. 5 (e) of the main text is $x + 10^{-8}A{\frac{3(-1+x)^2-a^2}{a^2+(-1+x)^2}}^3$ for $a = 0.045$ and $A = 1, 9, 25, 64, 100$, roughly mimicking a 100-fold increase of κ (10-fold increase in magnetic field).